Fiber-Optic Michelson Interferometer with Faraday Mirrors for Acoustic Sensing using a 3×3 Coupler and Symmetric Demodulation Scheme

Peter Lanier Gartland

Thesis submitted to the Faculty of the

Virginia Polytechnic Institute and State University

in partial fulfillment of the requirements for the degree of

Master of Science

in

Electrical Engineering

Anbo Wang, Chair

Ahmad Safaai-Jazi

Yizheng Zhu

September 9, 2016

Blacksburg, Virginia

Keywords: Fiber Optics, Michelson Interferometer, 3×3 Coupler, Acoustic Sensing

Fiber-Optic Michelson Interferometer with Faraday Mirrors for Acoustic Sensing using a 3×3 Coupler and Symmetric Demodulation Scheme

Peter Lanier Gartland

(ABSTRACT)

For the past 40 years, acoustic sensing has been a major avenue for the growth of interferometric fiber-optic sensors. Fiber-optic acoustic sensors have found uses in military, commercial, and medical applications. An interferometric fiber-optic acoustic sensor is presented utilizing the Michelson interferometer configuration with Faraday mirrors to eliminate polarization fading. A 3×3 coupler is used as the beamsplitting component, and a symmetric demodulation algorithm is applied to recover the phase signal. This sensor has a theoretical resolution of 5.5 pico-strains and room to improve. Such improvements are discussed in the conclusion.

Fiber-Optic Michelson Interferometer with Faraday Mirrors for Acoustic Sensing using a 3 × 3 Coupler and Symmetric Demodulation Scheme

Peter Lanier Gartland

(GENERAL AUDIENCE ABSTRACT)

For the past 40 years, acoustic sensing has been a major avenue for the growth of fiber-optic sensors. The optical fiber itself acts essentially like a microphone that is sensitive to acoustic emissions in the audible range up into the ultrasonic range. Because of the fiber's innate resistance to harsh environments, fiber-optic acoustic sensors have found uses in military, commercial, and, more recently, medical applications. The extremely high sensitivity achievable with a fiber-optic acoustic sensor is demonstrated using a simple arrangement of now readily available fiber-optic components and digital signal processing.

Dedication

This thesis is dedicated to my parents for their love and constant encouragement, knowing I would never blow it; to my brother Patrick, his wife Ashley, and my nephew Christopher for their love and laughter; to my friends for their conversation that kept me happy and sane; and to my dog Perrin and his best friend Lady.

Acknowledgments

I would like to give my sincerest thanks to Dr. Wang for giving me the opportunity to work and learn in the CPT after I decided to stop by his office one day. He was always a source of encouragement and creativity during the sometimes arduous days of graduate school. In addition, I would like to thank Dr. Safaai-Jazi and Dr. Zhu for teaching detailed courses that helped get me into the world of electromagnetics and fiber optics. I would also like to thank Li Yu for first showing me the ropes of the CPT and Dr. Haifeng Xuan for providing guidance for my work. My appreciation also extends to Bo Liu, Zhipeng Tian, Di Hu, Amiya Behera, and the rest of the CPTers for answering questions, offering help, and making the CPT a pleasant place to do work each day.

Contents

List of Figures

List of Tables

Chapter 1

Introduction

1.1 Fiber Optic Acoustic Sensing

Research on the acoustic sensitivity of optical fibers began in earnest in the late '70s and early '80s with much of the focus being on the development of fiber-optic hydrophones by the Naval Research Laboratory. They investigated different coatings for fibers and developed array-based hydrophone sensors [1]. Beginning around the '90s, another practical use for optical fiber acoustic sensors emerged in the form of partial discharge detection in high-power electric transformers [2]. A partial discharge refers to the electrical discharges that occur inside an aging transformer as the insulating oil breaks down. Fiber-optic sensors can detect the ultrasonic acoustic emissions given off by these discharges and even estimate the origin. More recently, fiber-optic acoustic sensors have been considered for use in medical applications, such as for ultrasonic imaging [3]. Thorough reviews on the advancements of optical fiber sensing, particularly interferometric sensing, are given in [4, 5, 6].

1.2   Background on Interferometry

An interferometer is a device that detects the relative phase between two interfering waves. At its heart, interference is a physical phenomenon explained by the concept of superposition, which says that two waves occupying the same space will add together. For electromagnetic waves in the form of light, in addition to occupying the same space, they must also satisfy two more conditions to produce a clear interference pattern. The first condition is that the two interfering waves must be coherent, that is, a definite phase relationship must exist between them. If the phase between the two light waves varies quickly and randomly, as in, say, sunlight, the resulting interference pattern will be washed out and appear as a constant intensity. For this reason, lasers, rather than broadband light sources, are typically used in interferometers; however, broadband light sources are still used in so-called white-light interferometry, but this technique was not used for this project. The second condition for interference to occur is that the two waves must share the same polarization. If the polarization between the two waves varies randomly, the interference pattern will fade in and out randomly too. This particular problem is solved by the use of Faraday mirrors to guarantee co-polarization of the light waves and is explained in Chapter 2.5. While practically all interferometers deal with electromagnetic waves, they nevertheless come in a variety of shapes and sizes. Several common interferometer topologies are shown below.

1.2.1   Interferometer Topologies

Four well-known topologies are the Mach-Zehnder, Michelson, Fabry-Perot, and Sagnac interferometers. Each of these topologies originated as a free-space interferometer where the light travels through air between the lenses, beamsplitters, and mirrors comprising the system. However, an important characteristic common among each of these topologies is that they are now easily implemented using fiber-optic components. Alignment is no longer an issue because the light is guided between components through optical fiber, which allows for

a much more robust system in terms of both size and stability. Fiber-pigtailed laser diodes eliminate the need for lenses; fiber couplers replace beamsplitters; and mirrors, along with just about every other optical device, are also available pigtailed to fiber. Diagrams of fiber-optic implementations of each of the above interferometers are shown in Figures 1.1 – 1.4. The fiber-optic Mach-Zehnder interferometer shown in Figure 1.1 splits the light into two
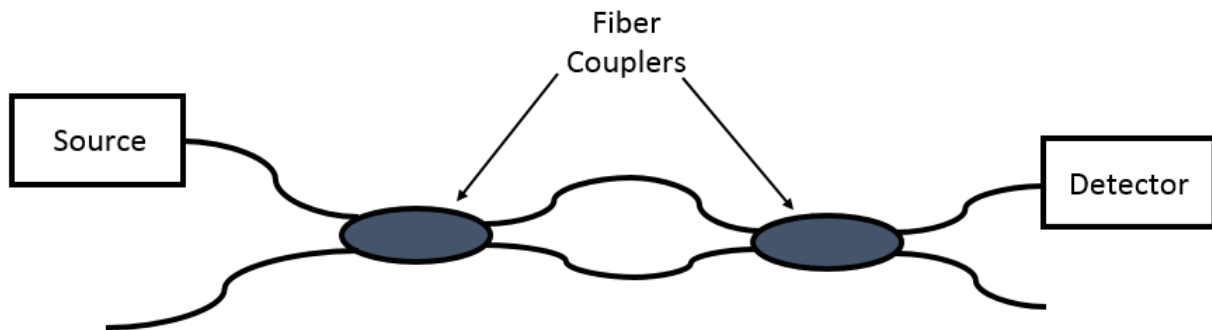
Figure 1.1: Mach-Zehnder: Light from a source is split into two paths and then recombined at a later point where interference takes place according to the phase difference accumulated along the different paths.

different arms, one of which is typically designated as the "sensing" arm with the other being the "reference" arm. The splitting is achieved by a fiber-optic directional coupler. The fiber making up the sensing arm is exposed to the environment, allowing the quantity of interest, the measurand, to alter certain properties of the fiber, such as length or refractive index. This will in turn alter the phase of the light passing through the sensing arm. Meanwhile, the reference arm is isolated from these effects, so when the two arms recombine in the second coupler, changes in the resulting interference pattern will reveal the accumulated phase difference. Similar to the Mach-Zehnder configuration, a Michelson interferometer splits the light into two separate arms with a directional coupler. However, instead of the arms recombining in a second coupler, mirrors reflect the light in each arm back to the original splitting point, which is where the interference will take place. Fiber-optic Fabry-Perot interferometers (FPIs) usually consist of a pair of closely-spaced reflectors. One of the reflectors is the cleaved end of an optical fiber, and the other reflector is either another fiber end or some
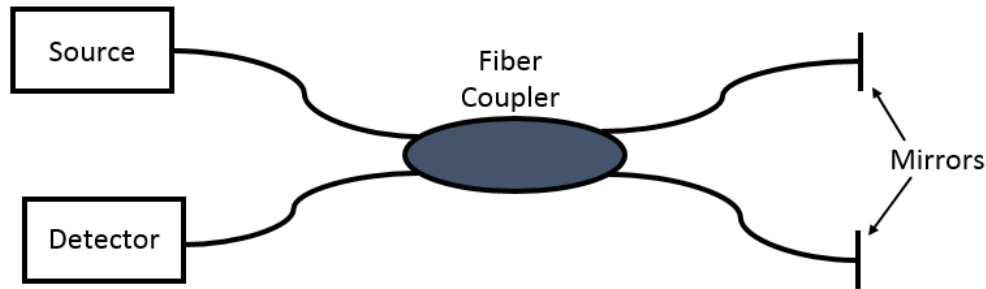
Figure 1.2: Michelson: Light from a source is split into two paths which are then reflected back by mirrors and allowed to interfere according to the phase difference accumulated along the different paths.

other structure that can reflect light. The cavity formed by the two reflectors is a physical path length difference between the two reflected beams and can be directly modulated by the environment to produce changes in the interference of the two reflections. For example, a diaphragms have been constructed on the end of an optical fiber that will bow in or out in response to pressure changes [7]. Fiber-optic FPIs can be made very small with cavity lengths on the order of micrometers and therefore make extremely compact point sensors. The Sagnac interferometer is unique in that it is sensitive to rotation about the axis of the loop. When counter-propagating light waves travel in a rotating frame, a phase difference develops between them. This phenomenon is known as the Sagnac effect and has been very successfully employed for the production of fiber-optic gyroscopes [8].

The interferometer topology used in this fiber-optic acoustic sensing system is the Michelson interferometer. Michelson interferometers have been responsible for some of the most important and necessarily sensitive measurements in history. One such example is the Michelson-Morely experiment conducted in 1887 which helped disprove the existence of a "luminiferous aether" through which light was thought to propagate. The Michelson interferometer, as the experimental configuration became known, was the original free-space version of the interferometer in Figure 1.2. In this setup, the interference pattern was viewed on a screen and consisted of evenly spaced, alternating light and dark vertical bars called "fringes." The
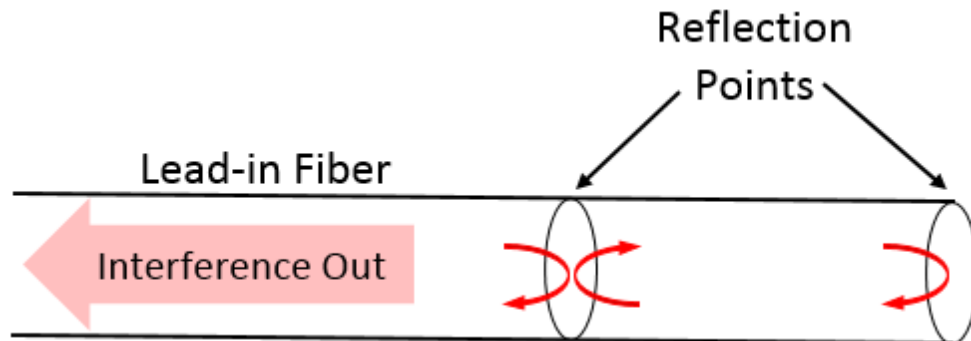
Figure 1.3: Fabry-Perot: Light is incident on two parallel, partially reflective surfaces. The multiple reflections from the near and far ends interfere according to the path length difference in the reflective cavity.

fringes shifted left or right in response to changes in the differential phase of the two interferometer arms. At the time of the Michelson-Morely experiment and after stabilizing the setup as much as possible, a change in the differential phase leading to a shift in the interference pattern was still expected to occur due to the relative motion of Earth through the aether; however, no such shift was observed.

Earlier this year, it was announced that gravitational waves were detected at the Laser Interferometer Gravitational-Wave Observatory (LIGO) [9], and the interferometer used was a Michelson configuration. While it adheres to the same concepts behind Michelson and Morely's setup, LIGO is no tabletop experiment: the perpendicular arms of the interferometer each stretch 4 km underground, maintain a vacuum through which the laser light travels, and support a multitude of stabilization components and environmental sensors to provide isolation from outside disturbances. The 4 km arms are necessary to achieve the required sensitivity, because the effect of gravitational strain is more pronounced on longer arms as they are stretched in one direction and compressed in the other. A passing gravitational wave modulates the differential length between the two arms of LIGO, which modulates the interference pattern and allows for detection.
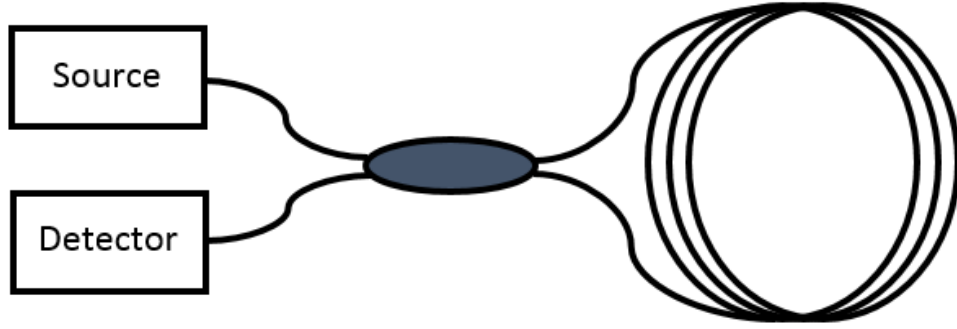
Figure 1.4: Sagnac: Light from a source is split into two arms, the ends of which are connected together to form a continuous loop. The counter-propagating waves then recombine and interfere at the output.

1.2.2 Two-beam Interference

For two electromagnetic (EM) waves traveling in the z-direction, their electric-field phasors, $\bar{E}_1$ and $\bar{E}_2$, may be written as

$$\begin{aligned}
\bar{E}_1 &= E_{01}e^{-j(\beta_{1z}z_1+\phi_{01})} = E_{01}e^{-j(\phi_1)} \\
\bar{E}_2 &= E_{02}e^{-j(\beta_{2z}z_2+\phi_{02})} = E_{02}e^{-j(\phi_2)},
\end{aligned} \tag{1.1}$$

where E_{01} and E_{02} are the electric field magnitudes, β_{1z} and β_{2z} are the propagation constants, z_1 and z_2 are the distances traveled by each wave, ϕ_{01} and ϕ_{02} are the initial phases, and ϕ_1 and ϕ_2 are the total phases of each wave. The total electric-field is given by the sum of $\bar{E}_1$ and $\bar{E}_2$: $\bar{E}_T = \bar{E}_1 + \bar{E}_2$. The intensity of an EM-wave is proportional to the magnitude-squared of its electric-field:

$$I_T \propto |\bar{E}_T|^2 = |\bar{E}_1 + \bar{E}_2|^2 = (\bar{E}_1 + \bar{E}_2)(\bar{E}_1 + \bar{E}_2)^*, \tag{1.2}$$

where * denotes the complex conjugate. Using Equation (1.1) in Equation (1.2) and taking the real part yields

$$I_T = I_1 + I_2 + 2\sqrt{I_1 I_2}\cos(\Delta\phi), \tag{1.3}$$

where $I_1 = E_{01}{}^2$, $I_2 = E_{02}{}^2$, and $\Delta\phi = \phi_1 - \phi_2$. Equation (1.3) may also be written in terms of the fringe visibility, η, which is defined as $(I_{MAX} - I_{MIN})/(I_{MAX} + I_{MIN})$. Inspecting

Equation (1.3) reveals $I_{MAX} = I_1 + I_2 + 2\sqrt{I_1 I_2}$ and $I_{MIN} = I_1 + I_2 - 2\sqrt{I_1 I_2}$, which leads to $\eta = 2\sqrt{I_1 I_2}/(I_1 + I_2)$. Equation (1.3) can then be expressed as

$$I_T = I_0(1 + \eta \cos(\Delta \phi)), \tag{1.4}$$

where $I_0 = I_1 + I_2$. The fringe visibility, which varies between 0 and 1, gives a measure of how close the waves are to achieving perfect constructive and destructive interference. When η is 1, the resulting intensity varies between 0 and twice of I_0, and as η approaches 0, the fringes become smaller and smaller until they disappear into the constant value of I_0. Maximum fringe visibility is achieved when $I_{MIN} = 0$, which requires that the two interfering waves have the same amplitude, or $I_1 = I_2$. Therefore, the power in the two interferometer arms should be made the same; or, looked at another way, the loss in the two arms should be equalized.

1.2.3   Polarization Signal Fading

The fringe visibility may also be degraded by a difference in the polarization state of the two waves. The effect of mismatched polarization states between the two interferometer arms may be accounted for by a cosine factor in the expression for fringe visibility:

$$\eta = \frac{2\sqrt{I_1 I_2}}{I_1 + I_2} \cos\left(\frac{\Theta}{2}\right), \tag{1.5}$$

where Θ is the angle between the two points on the Poincaré sphere corresponding to the polarization states of the two interfering waves [5]. The Poincaré sphere is a geometrical way of expressing the polarization state of EM waves, much like the Smith chart is a geometrical way of expressing complex impedances and their transformations. Note that Θ may vary between 0° and 180°, and consequently, the cosine factor in Equation (1.5) will vary between 1 and 0. EM waves occupying points on opposite sides of the Poincaré sphere ($\Theta = 180°$) force η to 0 and will not interfere with each other. These are referred to as orthogonal polarization states.

The fact that the relative polarization between two EM waves can cause the interference pattern to vanish has always presented a challenge to interferometry. The polarization of light traveling in a medium, such as glass or plastic, can change quite easily over short distances and depends on the properties of the medium. When discussing optical fibers, birefringence is the term used to describe the anisotropy of the fibers' refractive index, that is, to what extent the light sees a different refractive index for different polarizations. Polarized light can always be decomposed into two orthogonal, linearly polarized components, and one definition of birefringence is the difference between the refractive indices of the two components, for example $n_x - n_y$, where n_x and n_y are the refractive indices along the $x-$ and $y-$axes, respectively. The refractive index of the silica glass comprising optical fibers is ideally an isotropic material, but in general, it contains some amount of randomly distributed mechanical stresses left over from the fiber drawing process. These intrinsic stresses combined with impressed stresses from bends in the fiber result in a random distribution of birefringence along the fiber and cause random variations in the polarization of light traveling through it. If the polarization varies randomly in the two arms of the interferometer before recombining, their polarizations will match only some of the time. Consequently, interference will occur sporadically and results in what is called "polarization signal fading." This undesirable effect is remedied by the use of Faraday mirrors, which will be presented in Section 2.5.

Chapter 2

System Description and Operating Principles

2.1   System Overview

As stated above, this system is a Michelson interferometer that measures acoustic emissions using a coil of optical fiber as the acoustic transducer. A diagram of the complete system is shown in Figure 2.1. A fiber-coupled laser launches the light into a fiber-optic circulator, the through-path of which is connected to a 3×3 coupler with equal splitting ratios in each arm. Two of the arms of the 3×3 coupler act as connections to the sensing and reference arms of the interferometer, while the third arm is unused. Fiber-coupled Faraday rotator mirrors (FRM) are attached to the ends of the reference and sensing arms to reflect the light back to the 3×3 coupler where they will recombine and interfere. All three of the outputs on the left-hand side of the 3×3 coupler, including the one coming back through the third port of the circulator, are detected by photodetectors (PDs). The three PDs convert the received optical power into voltage signals that are then digitized and processed in a demodulation algorithm to determine the changes in phase between the two arms.
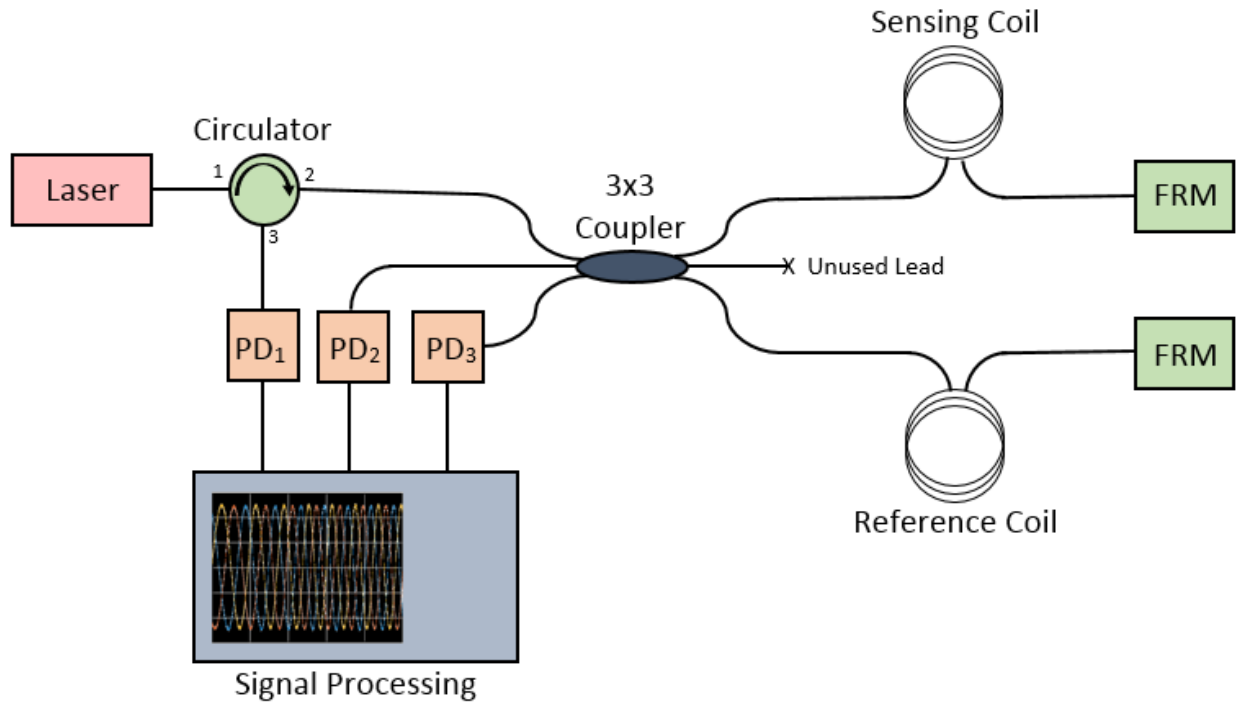
Figure 2.1: Diagram of the whole system.

2.2   Lasers

Two different lasers were primarily used when evaluating this system. A tunable laser (New Focus, Model 6328), and a distributed feedback (DFB) laser (Agere D2555Y31). They both operated close to 1550 nm. The tunable laser's output power was around -2.2 dBm, and the DFB laser's output power is close to 3 dBm. The tunable laser has a linewidth of less than 300 kHz over a period of 50 ms, while the DFB laser's linewidth is specified as typically 2 MHz, but guaranteed less than 10 MHz.

2.3   Circulator

The circulator's role is two-fold in this system. Its primary use is to provide access to one of the three outputs of the 3×3 coupler. The circulator is a three-port device (the ports are

labeled 1, 2, and 3 in Figure 2.1) that only allows a signal to travel in the direction indicated by the arrow. Light entering Port 1 will exit Port 2, and light entering Port 2 will exit Port 3. However, this circulator does not provide any path that exits Port 1, so any light entering Port 3 is simply lost inside the circulator. This asymmetry leads to its second role as an isolator to block any reflected light from making its way back into the laser cavity, which could cause severe stability issues and damage.

2.4 3×3 Coupler

The 3×3 coupler is the component that splits the light into two different arms, and it is where the reflected beams interfere with each other. The advantage a 3×3 coupler gives over a more conventional 2×2 coupler is that a passive demodulation scheme is possible with the three outputs of the 3×3 coupler. There are two useful expressions for the outputs of a 3×3 coupler when it is used in an interferometer. The first expression is more general because it allows for variations in the coupling coefficient and length of the coupling region [10]. The second expression is for the specific case of a symmetric 3×3 coupler that derives from the first [11]. A demodulation algorithm was proposed using each expression, but the symmetric demodulation algorithm [12], described in Chapter 3, was used for this system. The coupling coefficient expression and the symmetric expression are given in Equations (2.1) and (2.2), respectively.

$$P_I = -2D_2 \left(1 + \cos\phi\right)$$
$$P_{II} = D_1 + D_2 \cos\phi + D_3 \sin\phi \qquad (2.1)$$
$$P_{III} = D_1 + D_2 \cos\phi - D_3 \sin\phi$$

$P_{(I,II,III)}$ are the optical powers emerging from the three outputs of the 3×3 coupler, $D_{(1,2,3)}$ are three constants that depend on the coupling coefficients and the coupling length of the

three fibers, and ϕ is the phase difference between the two interferometer arms.

$$A_1 = C + B\cos\left(\phi\right)$$

$$A_2 = C + B\cos\left(\phi - 120°\right) \tag{2.2}$$

$$A_3 = C + B\cos\left(\phi + 120°\right)$$

This is the ideal expression for the outputs of a symmetric 3×3 coupler where there is a $120°$ phase difference between each of the outputs, and they all share the same amplitude and dc-offset. Deviations from these ideal values causes distortion in the demodulated signal and will be discussed in Chapter 3.

Figure 2.2 shows simulated 3×3 coupler outputs for several different input phase modulations. The simulated outputs help to give a rough idea of the type of phase modulation just by looking at the 3×3 coupler output. Note that in Figure 2.2a, the constant value of ϕ will determine the particular relative positions of the three outputs. This is seen clearly in the lab when viewing the outputs on a short time scale as they slowly vary. For example, imagine looking at a very thin window of Figure 2.2c and sliding horizontally.

2.5   Faraday Mirrors

As mentioned in the introduction, the state of polarization (SOP) of light in an optical fiber may vary wildly as it travels along a birefringent fiber, thus making stable interference unrealistic. Previously, the only way to reliably avoid polarization fading was to use polarization-maintaining (PM) fiber and polarization controllers. This solution often makes the resulting fiber-optic system too expensive for practical deployment; for example, PM fiber is around two orders of magnitude more expensive than conventional telecommunication fiber per meter. A simple method for eliminating the effects of birefringence on the polarization of light that retraces its own path, e.g., the arms of a Michelson interferometer, is to use Faraday mirrors as the reflectors [13, 14]. A Faraday mirror, now commonly available pigtailed with optical fiber, consists of a Faraday rotator followed by a mirror. A Faraday
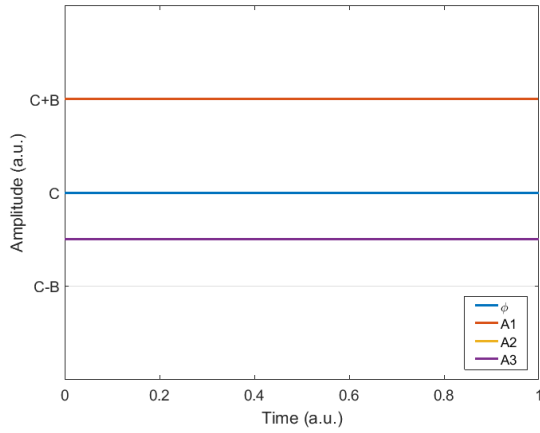
(a) *Constant ϕ.
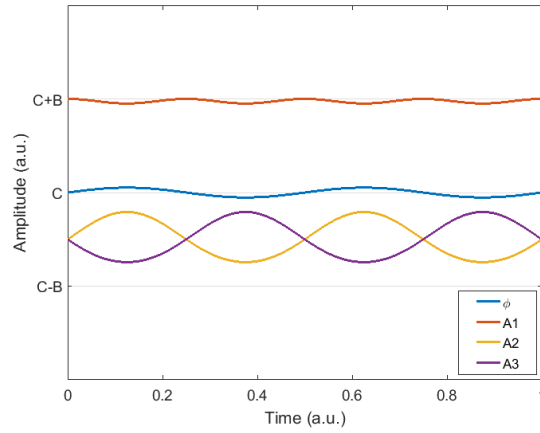
(b) Weak sinusoidal ϕ.
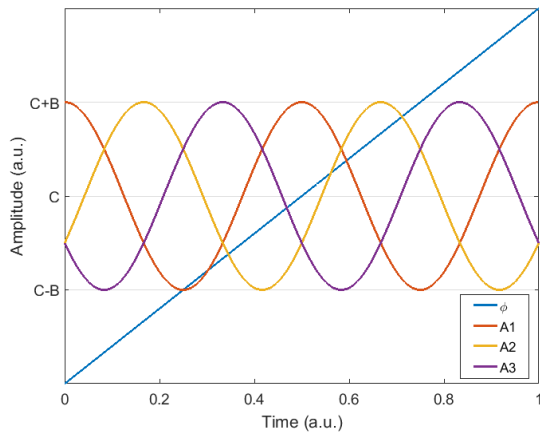
(c) Linear ϕ.
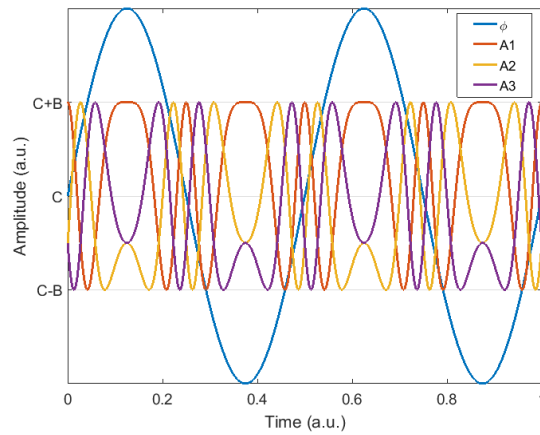
(d) Strong sinusoidal ϕ.

Figure 2.2: Simulated 3×3 coupler outputs for different input phase modulations (in blue). *Note that in (a), A2 and A3 are at the same value of $C - B/2$.
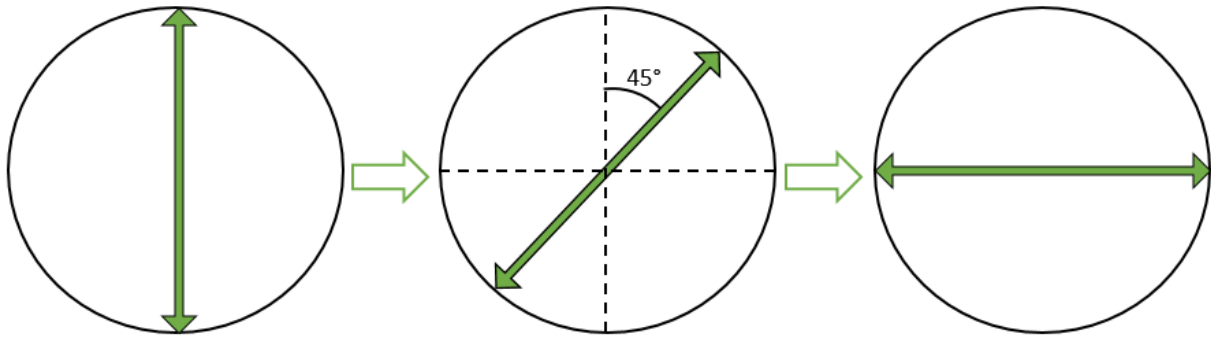
Figure 2.3: Faraday Rotation: the incident vertical polarization is rotated 45° on the first pass and then an additional 45° on the return pass.

rotator is a device that rotates the polarization of light passing through it by utilizing the Faraday effect, which is a magneto-optic effect that occurs when light propagates through a magnetic field. Qualitatively, the SOP is rotated by 45° during the first pass through the Faraday rotator, and after reflection, it is rotated another 45° on the return trip, resulting in a total rotation of 90° away from the initial SOP. Figure 2.3 shows the effect a Faraday mirror would have on light linearly polarized along the vertical axis. The doubling of the rotation angle from a forwards and backwards pass through a Faraday rotator demonstrates the nonreciprocal nature of the device, that is, the direction of rotation is independent of the light's direction of propagation; it only depends on the direction of the external magnetic field. This differentiates Faraday rotators from other polarization rotators, such as half-wave plates.

Another way to conceptually understand the Faraday effect is as a type of circular birefrin- gence. Since polarized light may also be expressed as the sum of two orthogonal, circularly polarized components, such as right-hand circularly polarized (RHCP) and left-hand cir- cularly polarized (LHCP) light, circular birefringence, by analogy with linear birefringence discussed in Section 1.2.3, will cause the RHCP and LHCP components of light to travel at different speeds and result in a rotation. It should be stressed, however, that the linear birefringence in the fiber results solely from the anisotropy of the silica glass and that the

circular birefringence results from the magnet in the Faraday rotator.

As for a mathematical description of Faraday mirrors and the polarization stabilization scheme, Jones matrices and vectors provide a useful formalism [13, 15]. A Jones vector can represent any SOP as a linear combination of two basis vectors, which may simply be chosen as linearly polarized light along the x- and y-axes. Therefore, the phasor, $\bar{\mathbf{E}}$, of light with an x- and y-component and a phase offset of θ can be simply written as a Jones vector:

$$\bar{\mathbf{E}} = E_{0x}\hat{\mathbf{x}} + E_{0y}e^{j\theta}\hat{\mathbf{y}} \implies \begin{bmatrix} E_{0x} \\ E_{0y}e^{j\theta} \end{bmatrix} \tag{2.3}$$

Jones matrices are 2×2 matrices that operate on a Jones vectors to alter the SOP. Each component in an optical system can be assigned a Jones matrix, and their product represents the total effect of the system on the SOP. First, the Jones matrix of the Faraday mirror itself will be derived. The Jones matrix corresponding to a rotation about the axis of propagation by an angle θ is given by

$$[R] = \begin{bmatrix} \cos\theta & \sin\theta \\ -\sin\theta & \cos\theta \end{bmatrix}, \tag{2.4}$$

and the Jones matrix for reflection at a mirror is given by

$$[M] = \begin{bmatrix} -1 & 0 \\ 0 & 1 \end{bmatrix} \tag{2.5}$$

$[M]$ may be viewed as inverting the x-dimension, just as looking into a mirror causes a right-handed person to appear left-handed. The net Jones matrix corresponding to a Faraday rotator mirror (FRM) is then given by

$$[FRM] = \begin{bmatrix} \cos\theta & \sin\theta \\ -\sin\theta & \cos\theta \end{bmatrix}_{\theta=-45°} \begin{bmatrix} -1 & 0 \\ 0 & 1 \end{bmatrix} \begin{bmatrix} \cos\theta & \sin\theta \\ -\sin\theta & \cos\theta \end{bmatrix}_{\theta=45°} = \begin{bmatrix} 0 & -1 \\ -1 & 0 \end{bmatrix}, \tag{2.6}$$

where the first rotation is assumed to be counter-clockwise ($+45°$), so the second rotation, from the light's perspective, should be clockwise ($-45°$). The Jones matrix representing the birefringent fiber can be modeled as a generic elliptic retarder, and, as shown in [14], when it

Table 2.1: Selected physical and optical properties of the fiber.

Core Diameter	8.2	μm
Cladding Diameter	125	μm
Coating Diameter	242	μm
Core Refractive Index	1.468	n/a

is traversed forwards and backwards with the FRM in the middle, the resulting polarization becomes constant and orthogonal to the original SOP. This means that no matter what the distribution of birefringence is along the separate arms of the Michelson interferometer, the evolution of their respective SOPs will always end up at the same point. Of course, the rate of change of the birefringence in the fiber must be slower than the round-trip travel time of the light so that the polarization can "unwind" to the correct state.

2.6 Fiber Coils

All of the fiber used in the system is conventional single-mode telecommunication fiber (Corning, Inc. SMF-28). Relevant optical and physical properties of the fiber are given in Table 2.1.

As will be seen in Equation (5.3), the acoustic responsivity is directly dependent on the length of the sensing fiber, therefore the sensitivity can be increased by exposing as much fiber to the acoustic field as possible. The limiting factors to the amount of fiber able to be used in the sensing head are the size of the coil and the target acoustic frequency. When the acoustic wavelength, λ_a, is much larger than the fiber coil's dimensions, the entire coil is subjected to approximately the same pressure at any given instant. However, if the acoustic wavelength is much smaller than the coil dimensions, there will be both pressure peaks and troughs present in the coil at the same time, which will tend to average each other out,

Table 2.2: Acoustic wavelengths in air and water at various frequencies.

f_a	λ_a in air ($c_a \approx 340$ m/s)	λ_a in water ($c_a \approx 1500$ m/s)
20 Hz	17 m	75 m
20 kHz	17 mm	75 mm
200 kHz	1.7 mm	7.5 mm
2 MHz	170 μm	750 μm

and the overall effect on the phase of the light will be lessened. For reference, Table 2.2 lists the wavelengths of acoustic emissions at various frequencies in air and water using the relationship $\lambda_a = c_a/f_a$, where λ_a, f_a, and c_a are the wavelength, frequency, and speed of sound, respectively. In air, λ_a becomes smaller than the diameter of the optical fiber's coating past around 1 MHz.

I constructed three fiber coils, two of which were targeted for use as sensors and the third primarily acting as the reference coil. There is no fundamental difference between the coils aside from their shape, so any of them could be used as the sensor or the reference. A picture of all three coils is given as Figure 2.4. The slinky-shaped coil in the center was hand-wound on a metal rod with the desired diameter. Before winding around the rod, it was wrapped in wax paper so that it could carefully slide out of the wax paper without disrupting the coil's shape. Additionally, two thin lines of glue were applied down opposite sides of the coil to maintain its shape. The "donut" coil on the right side of Figure 2.4 was constructed in a similar manner, except two spacers were fastened on the rod to confine the winding in the axial direction. The coil on the left in Figure 2.4 was mostly used as the reference coil and was simply wound around my hand. Rubber holders keep the donut and reference coils from unraveling. Table 2.3 summarizes the dimensions of the three coils. Each of the coils is made of close to 12 meters of fiber.
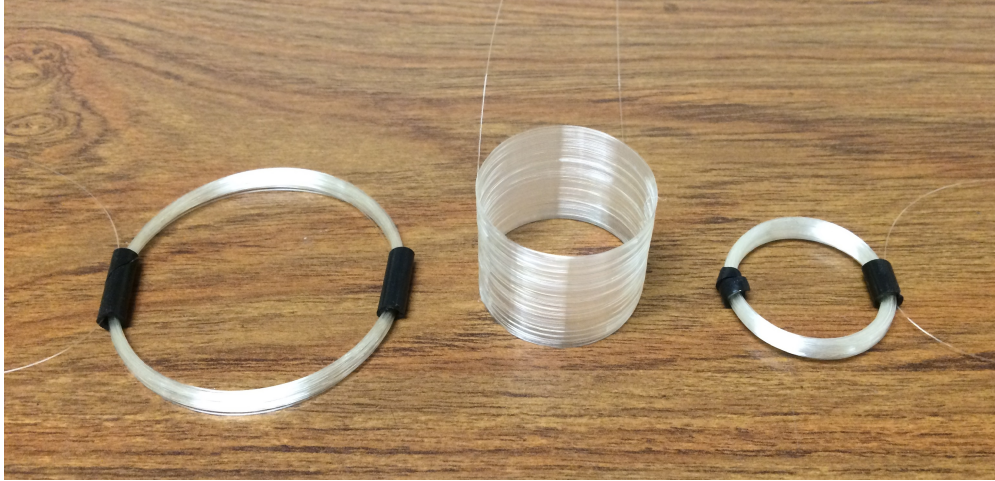
Figure 2.4: Three coils: each consists of approximately 12.75 m of fiber including the leads.

Table 2.3: Physical dimensions and characteristics of the fiber coils.

	Slinky	Donut	Reference	Units
Outer Diameter	34	34	59	mm
Inner Diameter	34	27	53	mm
OD – ID	1 fiber	7	6	mm
Coil Axial Length	26	4	4	mm
Fiber Length	12.75	12.75	12.75	m
Optical Loss	2.8	2.2	0.9	dB

Chapter 3

Signal Demodulation

A term at the heart of interferometry is demodulation, and it refers to the process of extracting the desired signal from the available information. The signal of interest is the phase difference between the two interferometer arms, but there is no "phase-meter" that can directly report this phase. Instead, the phase difference must be derived from a measurable quantity, which is the intensity of the light at the interferometer's output. When the phase difference is modulated by the environment, the output intensity will be modulated according to a relation similar to Equation (1.4). Before the advent of sophisticated optical detectors phase demodulation was commonly performed by inspecting the motion of the interference fringes. In free-space interferometers, the interferometric output is simply pointed to a wall or screen for viewing, and the phase difference can be monitored by counting the number of fringes that pass through a chosen point on the viewing screen. Each time two adjacent bright fringes or two adjacent dark fringes pass through the point, the phase between the arms has changed by 2π radians. The concept of counting fringes remains the basic idea behind interferometric demodulation, but improvements in detection technology, such as sensitive photodiodes, allow much smaller phase modulations to be detected. However, the fact that the output intensity is related to the cosine of the phase difference rather than being linearly related to it can sometimes hide small phase fluctuations. As the phase differ-

ence approaches a multiple of π, the slope of the cosine response approaches 0, meaning any changes will be small. This signal fading makes direct phase monitoring unreliable without demodulation.

Many different approaches exist for signal demodulation, several of which are described, for example, in [16]. One set of methods relies on an active control loop to maintain the phase difference at $\pi/2$ radians (at quadrature), which is the quasi-linear region of the cosine response. When only one output is available, the demodulated signal is taken as the error signal which tries to move the operating point away from the established $\pi/2$ radians. Another approach is to generate two output signals with a $\pi/2$ phase difference between them and then process these two signals appropriately to isolate the change in phase, $\Delta\phi$. This system uses the three outputs of the 3×3 coupler and some mathematical manipulations to obtain the demodulated phase.

3.1 Symmetric Demodulation Algorithm

The symmetric demodulation algorithm, first proposed at the Naval Research Laboratory [12], uses the 120° phase difference between the outputs of a 3×3 coupler to exploit some trigonometric identities and derive an expression directly proportional to the interferometric phase. Recall from (2.2) that the three outputs of the 3×3 coupler may be written as

$$A_i = C + B \cos \left[\phi - 120°(i - 1) \right] \qquad i = (1, 2, 3), \tag{3.1}$$

where A_i is the optical power arriving at the three photodetectors. First, the dc-offset is calculated as

$$C = \frac{1}{3} \left(A_1 + A_2 + A_3 \right), \tag{3.2}$$

which makes use of the trigonometric identity $\cos(x) + \cos(x - 120°) + \cos(x + 120°) = 0$. The dc-offset is then subtracted from the three signals:

$$a_i = A_i - C = B \cos \left[\phi - 120°(i - 1) \right] \qquad i = (1, 2, 3). \tag{3.3}$$

Next, the derivative of each signal is calculated:

$$\frac{da_i}{dt} = -B\dot{\phi}\sin\left[\phi - 120°(i-1)\right] \qquad i = (1,2,3), \tag{3.4}$$

where $\dot{\phi}$ is the derivative of ϕ. Now, the ith signal is multiplied by the difference between the other two derivatives:

$$a_i\left(\frac{da_{i+1}}{dt} - \frac{da_{i+2}}{dt}\right) = \sqrt{3}B^2\dot{\phi}\cos^2\left[\phi - 120°(i-1)\right] \qquad i = (1,2,3) \tag{3.5}$$

where $(i+3) \longleftrightarrow i$, and the trigonometric identity $\sin(x+y) - \sin(x-y) = 2\cos x \sin y$ was used. The $\cos^2$ dependence is then eliminated by summation with the trigonometric identity $\cos^2(x) + \cos^2(x-120°) + \cos^2(x+120°) = 3/2$:

$$\sum_{i=1}^{3}\sqrt{3}B^2\dot{\phi}\cos^2\left[\phi - 120°(i-1)\right] = \frac{3}{2}\sqrt{3}B^2\dot{\phi} \tag{3.6}$$

The right side of Equation (3.6) could be integrated now to get an expression proportional to ϕ, but it would also be proportional to B^2, which would make the output directly dependent on fluctuations in the laser power. This symmetric demodulation algorithm goes further to eliminate the B^2 dependence by summing the squares of a_i in Equation (3.3) to produce another quantity proportional to B^2:

$$\sum_{i=1}^{3}a_i^2 = \frac{3}{2}B^2. \tag{3.7}$$

Dividing the right side of Equation (3.6) by the right side of Equation (3.7) results in

$$\left(\frac{3}{2}\sqrt{3}B^2\dot{\phi}\right) \div \left(\frac{3}{2}B^2\right) = \sqrt{3}\dot{\phi}, \tag{3.8}$$

which can be integrated to produce the final demodulated phase:

$$\int \sqrt{3}\dot{\phi}dt = \sqrt{3}\phi. \tag{3.9}$$

3.2   Sources of Signal Distortion

The potential of signal distortion has been addressed [11] and the effects quantified to some extent [17]. The main sources of signal distortion are asymmetries in either the 3×3 coupler's

parameters or the three photodetectors. For example, the three outputs of the 3×3 coupler may not be exactly separated by $120°$, or each of the photodetector outputs may have different dc-offsets and amplitudes. Equation (2.2) can be rewritten as follows to account for these differences:

$$A_1 = C_1 + B_1 \cos{(\phi)}$$
$$A_2 = C_2 + B_2 \cos{(\phi - (120° + \delta_2))} \tag{3.10}$$
$$A_3 = C_3 + B_3 \cos{(\phi + (120° + \delta_3))}$$

Essentially, these asymmetries sabotage the trigonometric identities and other mathematical assumptions that the demodulation algorithm relies upon. The algorithm is not completely destroyed, but as shown in [11], artifacts manifesting as unwanted sinusoidal terms, will propagate through and appear at the output. An example of the asymmetries in the 3×3 coupler outputs and the resulting artifacts in the demodulated phase is shown in Figure 3.1. One advantage of using a digital system to perform the demodulation algorithm is that conditioning the sampled signals with, for example, a constant scale factor or dc-offset, is straight forward. Figure 3.1a shows the 3×3 coupler outputs directly from the photodetectors. The amplitudes vary quite markedly, and they have already been centered manually from the oscilloscope's front panel to equalize their dc-components. All of the different fiber connections and different amounts of bending between the 3×3 coupler and the photodetectors cause these discrepancies. For example, the smallest amplitude signal is the one that had to return through the circulator, which added additional loss. Figure 3.1c is the same capture as Figure 3.1a but with scaling factors applied to equalize the amplitudes. Figure 3.1b shows the demodulated phase of Figures 3.1a and 3.1c. The distortion is not very visible in Figure 3.1b, so Figure 3.1d plots the ratio of the demodulated phases to give a better idea of the distortion.
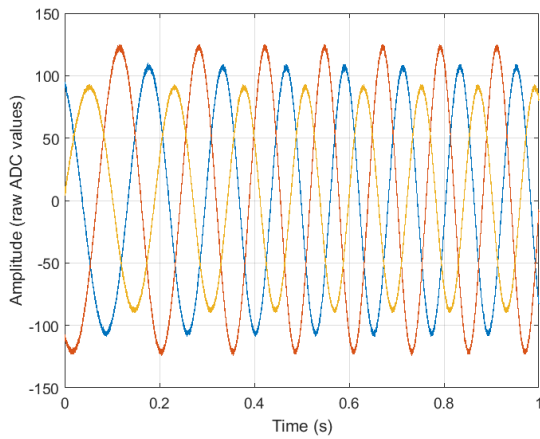
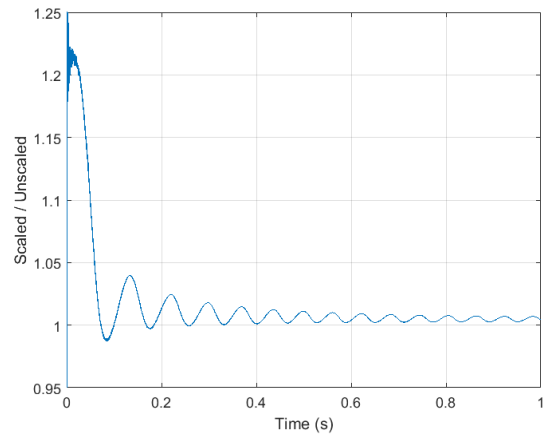(a) Asymmetric 3×3 coupler outputs.
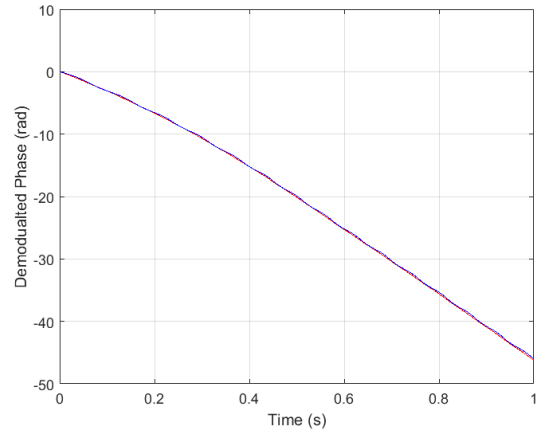
(b) Demodulated phases of scaled (red) and unscaled (blue).
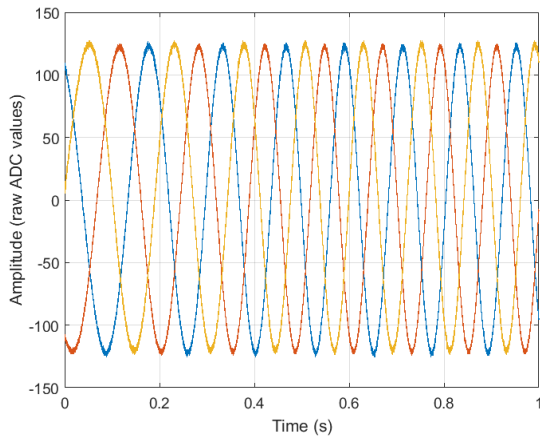
(c) Corrected 3×3 coupler outputs.

(d) Ratio of phases of scaled to unscaled.

Figure 3.1: Asymmetries in the 3×3 coupler outputs lead to distortion in the demodulated phase. The distortion can be reduced by digitally correcting the signals before applying the algorithm.

Chapter 4

Sources of Noise

As with any sensor, it is bound to pick up some amount of unwanted signal originating either from the surrounding environment or from within the sensor system itself. All such unwanted signals are considered noise in the sensors output. Environmental noise must usually be handled on a case-by-case basis because of the wide variety of applications and locations in which a sensor may be used. The noise from these environments may be minimized in a number of ways, for example, by properly isolating the sensor head from vibrations or temperature fluctuations, or it could be solved in signal processing by filtering out unwanted frequency components. As an example of the profound effect environmental noise can have, Figures 4.2 – 4.4 show the outputs of the sensor resting open to the air on the lab bench, enclosed in a box resting on the lab bench, and enclosed in a box suspended by rubber bands above the lab bench. A picture of the enclosed system is shown in Figure 4.1.

In addition to environmental noises, which may or may not be avoidable, every sensor is also subject to noise originating from the sensor itself. In this interferometer system, the noises can be separated into optical noise sources and electrical noise sources, both of which find their way through the system and manifest themselves as an unwanted signal at the output of the sensor.
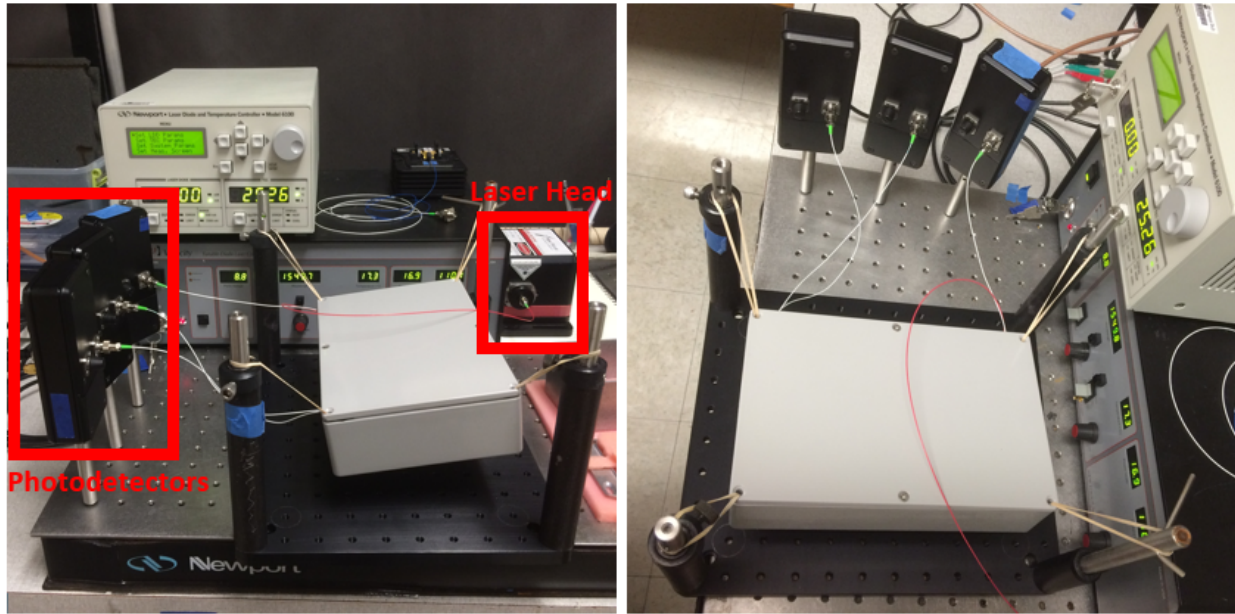
Figure 4.1: Two perspectives of the enclosed and suspended box used to isolate the fiber-optic components.

4.1   Electrical Noise Sources

All of the electronics that are used in the sensor system, which include the photodiodes and transimpedance amplifiers (TIAs), produce their own noise that is added to the three outputs used in the demodulation algorithm. The one noise present in all electrical instruments is Johnson noise (also known as Nyquist or thermal noise) and is caused by the random, thermally agitated motion of electrons in conductors. Johnson noise is often modeled as a series combination of a load resistance and a voltage source, whose output has a power spectral density (PSD) equal to

$$\frac{v_{th}^2}{\Delta f} = 4kTR, \tag{4.1}$$

where Δf is the measurement bandwidth, $k \approx 1.38 \times 10^{-23}$ J/K is the Boltzmann constant, T is the temperature in Kelvin, and R is the equivalent resistance of the load. The square-root of v_{th}^2 represents the standard deviation of the noise voltage fluctuations. Johnson noise is a white noise, which means its PSD, as seen in Equation (4.1), is a constant for all practical
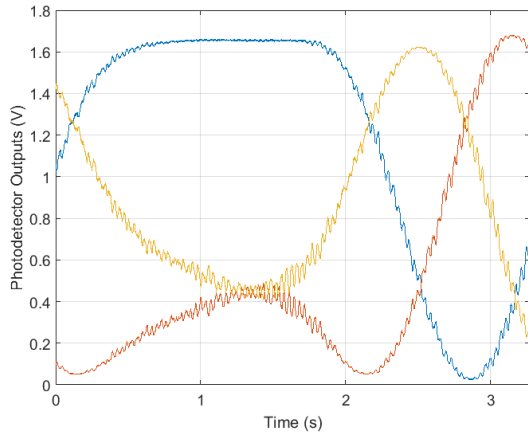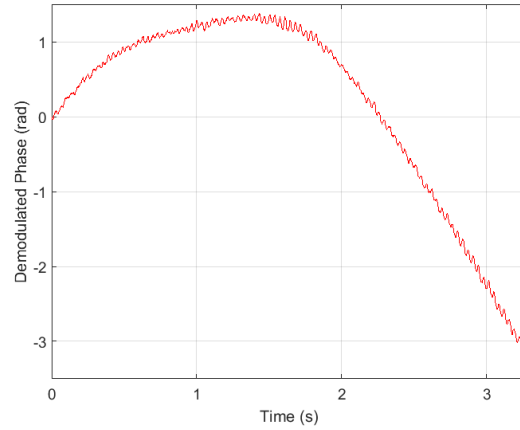
(a) Photodetector outputs.   (b) Demodulated phase.

Figure 4.2: Environmental noise for the open box on the lab bench.

(a) Photodetector outputs.   (b) Demodulated phase.

Figure 4.3: Environmental noise for the enclosed box on the lab bench.

(a) Photodetector outputs.

(b) Demodulated phase.
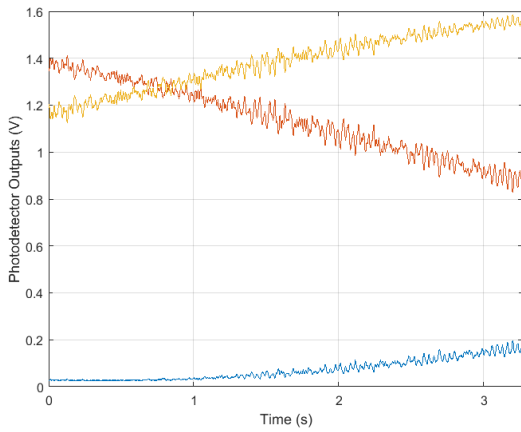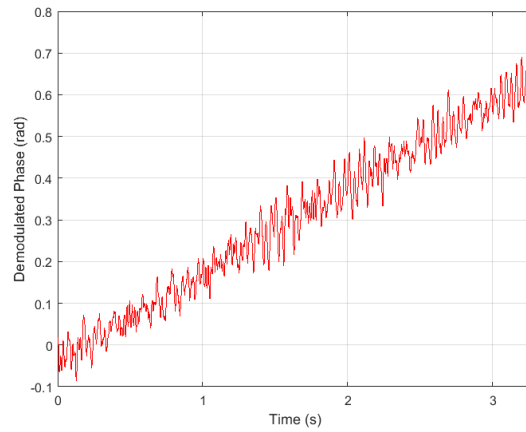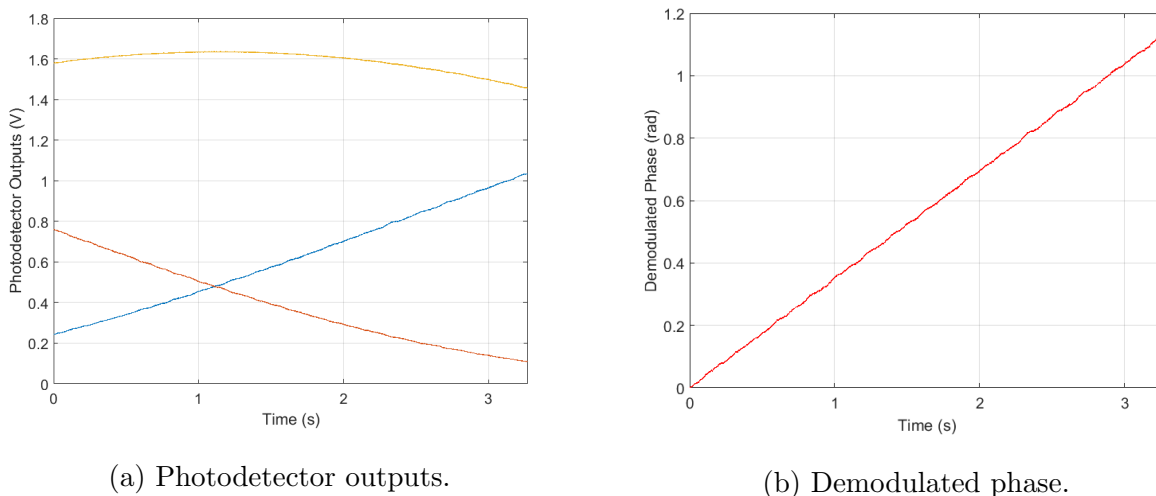
Figure 4.4: Environmental noise for the enclosed box suspended by rubber bands.

frequencies of interest. Sources of electronic noise in the photodetectors are the TIA and the shot noise of the photodiode. The TIA's gain comes from a large resistance, which can make its thermal noise significant. Additionally, the transistors that make up the rest of the amplifier produce their own noises, which are a combination of thermal noise and current noises. Modeling the noise of a given amplifier requires detailed knowledge of the circuit layout, so the manufacturer usually summarizes the noise performance with the noise figure (NF) of the amplifier. The NF, given in units of dB, relates the output signal-to-noise ratio (SNR) to the input SNR as

$$NF = 10 \log \left(\frac{SNR_{in}}{SNR_{out}} \right), \tag{4.2}$$

so it is a measure of how much noise the amplifier adds to the system. The shot noise in the photodiode arises from the quantum nature of light and manifests itself as current noise in the photodetection process. The measured noisy photocurrent can also be described by a PSD:

$$\frac{i_{shot}^2}{\Delta f} = 2qI_0, \tag{4.3}$$

where Δf is again the measurement bandwidth, q is the charge of an electron, and I_0 is the average photocurrent. The photodetectors used in this system were New Focus Model 2117

Photoreceivers, which include a band-pass filter and an additional amplifier together in a single package. Rather than specifying the NF for each of these components, New Focus provides a different figure to quantify the overall noise performance of the photodetector: the noise equivalent power (NEP). Conceptually, the NEP is the optical power required to produce (in a hypothetical noiseless device) the actual noise observed at the photoreceiver output. In other words, it is the optical power that would result in an SNR of 1. It is therefore given in units of $\mathrm{mW}/\sqrt{Hz}$, as it does depend on frequency like the individual thermal and shot noises.

4.2 Optical Noise Sources

Optical noise originates almost exclusively from the optical source used to excite the system. In this case, the optical source is a laser diode, and specific characteristics of the noise can vary markedly from laser to laser. However, just two quantities, namely relative intensity noise (RIN) and the laser's linewidth, are used to define the noise performance of lasers. RIN is a measure of the intensity fluctuations of the laser output, and the linewidth of a laser indicates how much the optical frequency fluctuates. Both RIN and the finite linewidth of a laser are the result of spontaneous emission, which is by nature a wideband and noisy process, but it still occurs in combination with the desired stimulated emission. Vibrations and temperature fluctuations in the laser cavity can also contribute to noise in the laser's output [18].

4.2.1 Laser Intensity Noise

Intensity noise in a laser is the random fluctuations of a laser's output power around its average value. The RIN of a laser quantifies this noise and can be written as the ratio

$$RIN = \frac{\delta P(t)}{\langle P(t) \rangle}, \tag{4.4}$$

where $\delta P(t) = P(t) - \langle P(t) \rangle$ is the power fluctuations away from the average laser output power, $\langle P(t) \rangle$. RIN is usually specified in db/Hz for some bandwidth. The RIN specification given for a DFB laser similar to the one used in this system is -160 dB/Hz in the bandwidth 20 MHz to 1 GHz, however the acoustic frequencies of interest are well below even 1 MHz, so this figure is not necessarily helpful for this application.

4.2.2   Laser Frequency Noise

Laser frequency noise is very important in interferometry, because it translates directly to output phase noise. The frequency noise originates from the laser itself and stems from the fact that the output light is not a single wavelength but a narrow range of wavelengths. This range of wavelengths (or frequencies) is called the linewidth of the laser and is usually taken at the full-width, half-maximum (FWHM) value of its output spectrum. The linewidths of lasers are often very narrow and so are usually reported in terms of frequency rather than wavelength, which makes the units more convenient, e.g. MHz versus femtometers or kHz versus attometers. The effect that a finite linewidth has on the output phase difference, $\Delta\phi$, of an interferometer can easily be shown by considering light with a nominal free-space wavelength of λ traveling in a material with an index of refraction of n and a path length difference of ΔL:

$$\Delta\phi = \frac{2\pi n \Delta L}{\lambda} = \frac{2\pi n \Delta L f}{c}, \tag{4.5}$$

where f is the frequency of the light, and c is the speed of light, and the relation $\lambda = c/f$ was used. Fluctuations in the frequency, δf, then translate directly to fluctuations in the phase, $\delta\phi$, as shown in Equation (4.6).

$$\delta\phi = \frac{2\pi n \Delta L \delta f}{c} \tag{4.6}$$

Notice, however, that the phase is also directly dependent on the path length difference, ΔL. If ΔL is made to be exactly 0, then the frequency noise of the laser would have no effect on the output phase of the interferometer. This is because, in the absence of a signal, the

light in both arms of the interferometer will travel the exact same distance and will therefore recombine exactly in phase, regardless of the wavelength. Now imagine a finite path length difference but with no laser frequency noise; the light in one arm will have to travel many more wavelengths compared to the other, so the light in the two arms will not necessarily arrive in phase, but the phase difference will be constant as long as the wavelength does not change. When the optical frequency varies randomly in addition to there being a path length difference, the output phase difference will vary randomly too, because all the optical frequencies that make up the linewidth will advance in phase at slightly different rates.

4.3   Arm Length Difference Reduction

As seen in Equation (4.6), the phase noise is directly proportional to the interferometer arm length difference, ΔL. I therefore sought to reduce the path length difference so that laser frequency noise would not be a limiting noise factor. The process of shortening the arm length difference started with use of an optical time-domain reflectometer (OTDR) (Opto-Electronic Inc., Model OFM130), which can measure the length of optical fiber with a precision of about ± 1 mm. The accuracy of the absolute length measurement was not important to me since I was only interested in the difference between two lengths. Once the length difference was known, I broke the longer arm and cleaved both ends using a linear motion stage attached to a micrometer to measure the amount of fiber I was cutting off. The two newly cleaved ends were then spliced back together with a fusion splicer (Fujikura, Model FSM-45PM). The whole process often took several attempts since a bad cleave or splice would either require shortening the longer arm or splicing additional fiber onto the shorter arm that could then be cleaved down to the correct length. The absolute length difference can be measured very accurately by looking at the spacing of the interference fringes when the interrogating light is swept over a range of wavelengths. This was accomplished with Micron Optics' sm-125 Optical Sensing Interrogator, which we simply call the "CTS." Figures 4.5 and 4.6 show the interference fringes produced when the "slinky" and "donut" coils are used in the

interferometer, respectively. The length difference can be derived by first considering the

Figure 4.5: Approximately 47 interference fringes produced by the "slinky" coil when sweeping the laser wavelength from 1540 nm to 1560 nm.

fringe order, N, of the interference, which is essentially the number of wavelengths or 2π phase shifts that occur in the arm length difference. Starting with the expression of phase difference from Equation (4.5),

$$\Delta\phi = \frac{2\pi n \Delta L}{\lambda} = 2\pi N, \tag{4.7}$$

a change in the fringe order, ΔN, can be written as

$$\Delta N = -\frac{2\Delta L n}{\lambda^2}\Delta\lambda, \tag{4.8}$$

where the factor of 2 comes from the fact that light travels the same path twice in a Michelson interferometer, and the negative sign can be ignored if just the absolute difference in length is desired. The output spectrum of the CTS allows us to count the fringes, so the path
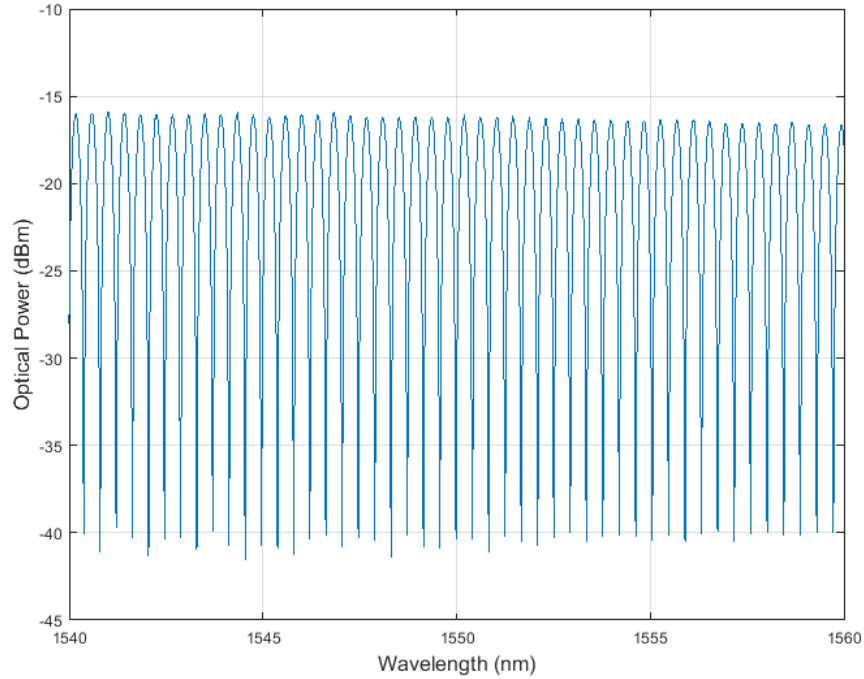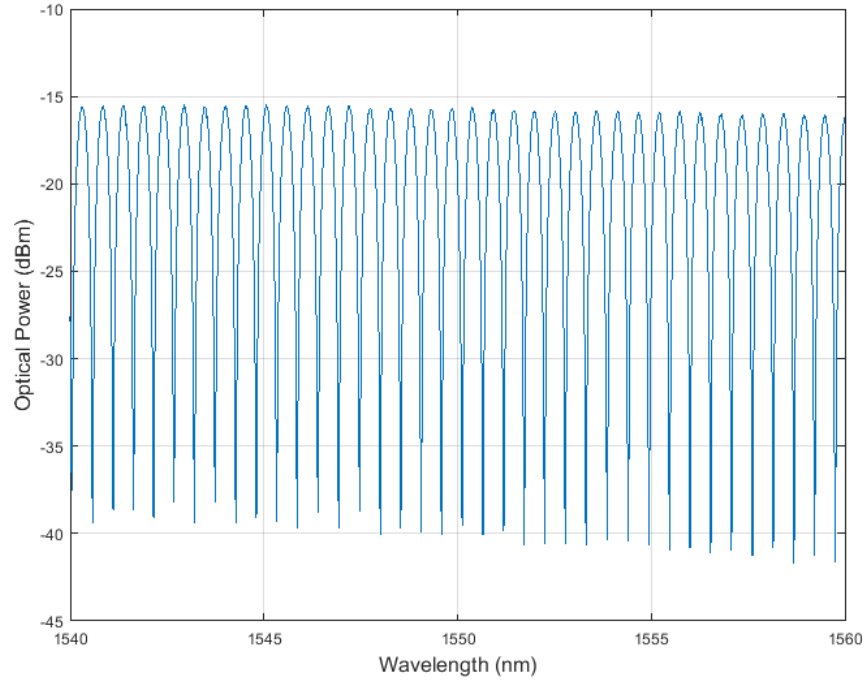
Figure 4.6: Approximately 37.5 interference fringes produced by the "donut" coil when sweeping the laser wavelength from 1540 nm to 1560 nm.

length difference is given as follows:

$$\Delta L = \frac{\Delta N \lambda^2}{2n\Delta\lambda}. \tag{4.9}$$

Using the values in Figures 4.5 and 4.6 for ΔN, $\lambda = 1550$ nm, $n = 1.468$, and $\Delta\lambda = 20$ nm, the calculated values of ΔL for the slinky and donut coils are 1.9 mm and 1.5 mm, respectively. Note that this value of ΔL is only achieved with respect to the reference coil when either the slinky or donut coil is attached a specific way in the system.

Chapter 5

Sensitivity Estimation

5.1 Theoretical Sensitivity in Terms of Strain

In the 1970s, much work was done investigating the theoretical sensitivity of optical fibers to acoustic waves in terms of pressure changes [19, 20]. The effect that acoustic waves have on the phase of light in an optical fiber can be explained by two fundamental mechanisms: changes in the physical length of the fiber and the strain-optic effect. The strain-optic effect is the change in the refractive index of a material due to applied stresses from, in this case, a passing acoustic wave [21]. Both of these effects directly impact the phase of light, ϕ, which is given by Equation (5.1) after traveling a distance L. The following was derived in [21].

$$\phi = \beta L = knL \tag{5.1}$$

The propagation constant, β, may be expressed as kn, where n is the index of refraction in the fiber, and $k = 2\pi/\lambda$ is the wavenumber with λ being the wavelength of the light. A change in the phase, $\Delta\phi$, may be written as

$$\Delta\phi = \Delta\beta L + \beta\Delta L, \tag{5.2}$$

where they first term is due to the strain-optic effect and the second term shows the actual change in length. $\Delta\beta$ was shown to largely depend on the change in the refractive index,

Δn, which is derived from the change in the optical indicatrix by applying the strain-optic tensor to the longitudinal strain in the fiber [21]. The final expression was given as

$$\Delta\phi = \epsilon L\beta - \frac{1}{2}\epsilon L\beta n^2 \Big[(1-\nu)p_{12} - \nu p_{11}\Big], \tag{5.3}$$

where ϵ is the strain, ν is Poisson's ratio of silica glass, and p_{11} and p_{12} are elements of the strain-optic tensor. Using Table 2.1 and the following values, $L = 24$ m (from the double pass through the 12 m arms), $\lambda = 1550$ nm, $\nu = 0.17$, $p_{11} = 0.12$, $p_{12} = 0.27$ [22], the theoretical change in phase per unit strain is approximately $\Delta\phi/\epsilon \approx 1.1 \times 10^8$ rad. While this result is a valid estimation for bare fiber, the protective coating that covers modern fiber has been shown to enhance the fiber's acoustic sensitivity by as much as an order of magnitude or more [23]. The coating's larger Poisson's ratio and compressibility make it more susceptible to deformation than silica glass, so when an acoustic wave impacts the fiber, the coating tends to pull the glass along with it more than the glass would alone [20].

In order to establish a limiting floor to the sensitivity of this particular sensor system, the minimum phase deviation was measured with the system enclosed in a box and suspended by rubber bands. This phase signal corresponds to a "noise equivalent strain," similar to the NEP defined in Chapter 4.1, that is, the amount of strain that would equivalently produce the observed noise. The standard deviation of the demodulated phase was measured for several cases in order to determine the minimum detectable strain as well as to give some insight into the effects of the noise. Figure 5.1 shows the noise data plotted for both the slinky and donut coils. The DFB laser and the tunable laser were used, two different arm length differences were used, and it was all plotted at different bandwidths. Using these minimum detectable phases in Equation (5.3) and solving for ϵ will give an estimate for the limit of the minimum detectable strain by this system. For example, the smallest standard deviation of phase was 0.6 mrad for the donut coil using the DFB laser and a path length difference of 1.5 mm; this corresponds to a "noise equivalent strain" of about 5.5 pico-strains.
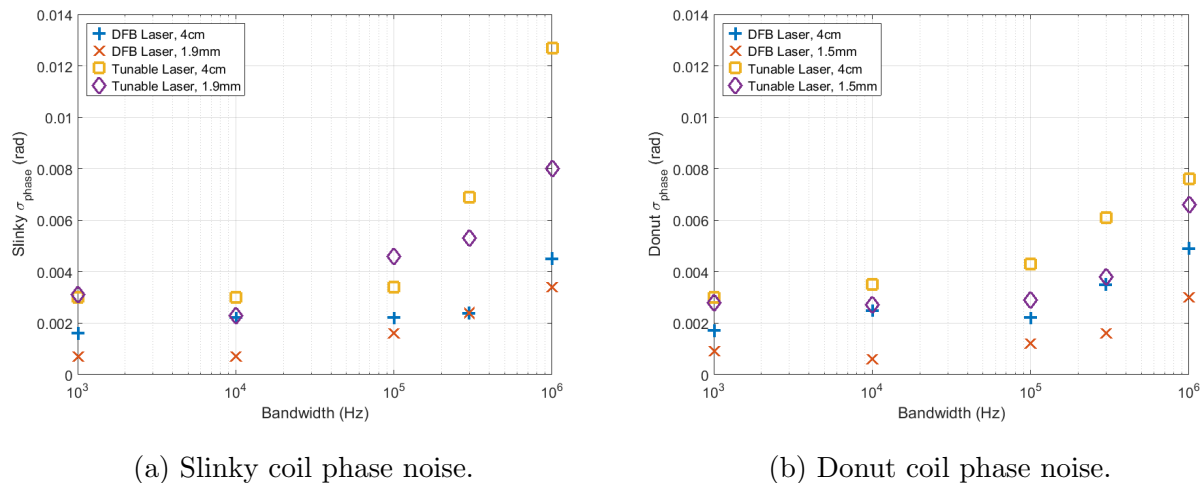
(a) Slinky coil phase noise.   (b) Donut coil phase noise.

Figure 5.1: Standard deviation of demodulated phase for each coil with different lasers and arm length differences.

5.2   Sensitivity Limitations

Figure 5.1 provides some interesting insight into the noise characteristics of the system. First notice that almost every noise measurement increases with the bandwidth, as expected. There are a couple exceptions that seemed to occur only when the bandwidth was 10 kHz. This was assumed to be a quirk of the photodetectors. Now, consider laser frequency noise: in almost every case, the shorter path length difference has a smaller noise value than the longer one. Equation (4.6) shows that the noise fluctuations are directly proportional to the path length difference. The noise obviously does not increase by the same factor as the path length, so the laser frequency noise is not the limiting noise source. However, in every case, the tunable laser's noise is larger than the DFB laser. This is likely a result of a combination of factors. For one, the tunable laser's output power was about 10 dB less than the DFB laser. This required the additional gain on the photodetectors to be set 100 times higher, which no doubt added more Johnson noise. The tunable laser may also exhibit more intensity noise than the DFB laser, however the RIN was not specified for either laser.

One of the limits to sensitivity estimation did not come from noise or the interferometer

side of the system; it came from the digital signal processing side. Initially, the analog-to-digital conversion took place in the 8-bit analog-to-digital converters (ADC) on board a high speed digital storage oscilloscope (LeCroy, DDA-260). 8-bits only provides 256 levels of quantization for a voltage swing close to 2 V, which corresponds to nearly 8 mV per quantization step if the full scale is used. This coarse quantization set another fundamental limit on the resolution of the photodetector voltages and therefore the demodulated phase. The sensitive noise measurements were therefore taken with a 16-bit ADC card (Gage, Razor X), which provides 2^8 times more quantization levels than the oscilloscope. This increase in voltage resolution allowed the phase noise measurements in Figure 5.1 to be taken.

Chapter 6

Future Work and Considerations

As mentioned in Chapter 5, the protective polymer coating on silica fibers acts to enhance the acoustic sensitivity. The supple nature of plastics, quantified by large Poisson ratios, allows acoustic waves to deform them more than glasses. Because the silica fiber and the protective coating are firmly attached, the overall Poisson ratio of the fiber is effectively increased. It has been shown that all-polymer optical fibers may achieve an order of magnitude increase in acoustic sensitivity for the same length, or they may provide the same sensitivity in a more compact sensing head [3]. The newly up-and-running fiber draw tower at the CPT may provide appropriate fiber for use in an acoustic sensor.

Additionally, in the interest of increasing sensitivity to slightly higher acoustic frequencies, reduced-diameter fiber may be substituted to reduce the size of the coils. However, reduced-diameter fiber will drive up the cost of the system considerably.

Instead of the sensor head being coils, altering their shapes could be beneficial for certain applications. For example, a flat, circularly shaped sensing head could be useful. It could be attached to some surface, or shaped in such a way to match the wavefront of a near-field acoustic source.

The "improved" demodulation techniques described in [11] may help eliminate the need to

condition the data during signal processing.

Finally, a calibrated microphone could be used to accurately determine this sensor's pressure-to-phase response and sensitivity, rather than relying solely on the theoretical sensitivity.

Bibliography

[1] J. H. Cole, C. Kirkendall, A. Dandridge, G. Cogdell, and T. G. Giallorenzi. Twenty-five years of interferometric fiber optic acoustic sensors at the naval research laboratory. *Washington Academy of Science Journal*, 90(3):40–57, 2004.

[2] A. K. Lazarevich. Partial discharge detection and localization in high voltage transformers using an optical acoustic sensor. Master's thesis, Virginia Polytechnic Institute and State University, 2003.

[3] D. Gallego and H. Lamela. High-sensitivity ultrasound interferometric single-mode polymer optical fiber sensors for biomedical applications. *Optics Letters*, 34(12):1807–1809, 2009.

[4] A. D. Kersey. A review of recent developments in fiber optic sensor technology. *Optical Fiber Technology*, 2(36):291–317, 1996.

[5] C. K. Kirkendall and A. Dandridge. Overview of high performance fibre-optic sensing. *Journal of Physics D-Applied Physics*, 37(18):R197–R216, 2004.

[6] G. Wild and S. Hinckley. Acousto-ultrasonic optical fiber sensors: Overview and state-of-the-art. *Ieee Sensors Journal*, 8(7-8):1184–1193, 2008.

[7] M. Han, X Wang, J. Xu, K. L. Cooper, and A. Wang. Diaphragm-based extrinsic fabry-perot interferometric optical fiber sensor for acoustic wave detection under high background pressure. *Optical Engineering*, 44(6), 2005.

[8] H. C. Lefevre. *The Fiber-Optic Gyroscope.* Artech House, 2nd edition, 2014.

[9] B. P. Abbot and et. al. Observation of gravitational waves from a binary black hole merger. *Physical Review Letters*, 116(6), 2016.

[10] S. K. Sheem. Optical fiber interferometers with [3by3] directional-couplers - analysis. *Journal of Applied Physics*, 52(6):3865–3872, 1981.

[11] Z. Q. Zhao, M. S. Demokan, and M. MacAlpine. Improved demodulation scheme for fiber optic interferometers using an asymmetric 3 x 3 coupler. *Journal of Lightwave Technology*, 15(11):2059–2068, 1997.

[12] D. A. Brown, C. B. Cameron, R. M. Keolian, D. L. Gardner, and S. L. Garrett. A symmetrical 3x3 coupler based demodulator for fiber optic interferometric sensors. *Fiber Optic and Laser Sensors Ix*, 1584:328–335, 1991. Proceedings of the Society of Photo-Optical Instrumentation Engineers (Spie).

[13] M. Martinelli. A universal compensator for polarization changes induced by birefringence on a retracing beam. *Optics Communications*, 72(6):341–344, 1989.

[14] A. D. Kersey, M. J. Marrone, and M. A. Davis. Polarization-insensitive fiber optic michelson interferometer. *Electronics Letters*, 27(6):518–520, 1991.

[15] E. Hecht. *Optics.* Addison Wesley, 4th edition, 2002.

[16] S. K. Sheem, T. G. Giallorenzi, and K. Koo. Optical techniques to solve the signal fading problem in fiber interferometers. *Applied Optics*, 21(4):689–693, 1982.

[17] S. T. Shih, M. H. Chen, and W. W. Lin. Analysis of distortion of a fiber optic michelson interferometric sensor caused by the imperfect properties of its 3x3 coupler. *Optical Engineering*, 36(7):2101–2106, 1997.

[18] R. Paschotta, H. R. Telle, and U. Keller. *Noise of Solid-State Lasers*, chapter 12, pages 473–510. CRC Press, 2007.

[19] B. Culshaw, D. E. N. Davies, and S. A. Kingsley. Acoustic sensitivity of optical-fibre waveguides. *Electronics Letters*, 13(25):760–761, 1977.

[20] J. A. Bucaro and T. R. Hickman. Measurement of sensitivity of optical fibers for acoustic detection. *Applied Optics*, 18(6):938–940, 1979.

[21] C. D. Butter and G. B. Hocker. Fiber optics strain-gauge. *Applied Optics*, 17(18):2867–2869, 1978.

[22] H. Zhang and P. R. Herman. 3d bragg grating waveguide devices. In R. Osellame, G. Cerullo, and R. Ramponi, editors, *Femtosecond Laser Micromachining Photonic and Microfluidic Devices in Transparent Materials*, chapter 9, page 254. Springer, 2012.

[23] B. Budiansky, D. C. Drucker, G. S. Kino, and J. R. Rice. Pressure sensitivity of a clad optical fiber. *Applied Optics*, 18(24):4085–4088, 1979.